JACS
JOURNAL OF THE AMERICAN CHEMICAL SOCIETY

Article

pubs.acs.org/JACS

Collective In-Plane Molecular Rotator Based on Dibromoiodomesitylene π-Stacks

Jun-ichi Ichikawa,[†] Norihisa Hoshino,[†,‡] Takashi Takeda,[†,‡] and Tomoyuki Akutagawa*[,†,‡]

[†]Graduate School of Engineering, Tohoku University, Sendai 980-8579, Japan

[‡]Institute of Multidisciplinary Research for Advanced Materials (IMRAM), Tohoku University, 2-1-1 Katahira, Aoba-ku, Sendai 980-8577, Japan

Supporting Information

ABSTRACT: Interest in artificial solid-state molecular rotator systems is growing as they enable systems to be designed for achieving specific physical functions. The phase transition behavior of four halomesitylene crystals indicated dynamic in-plane molecular rotator characteristics in dibromoiodomesitylene, tribromomesitylene, and dibromomesitylene crystals. Such molecular rotation in diiodomesitylene crystals was suppressed by effective I···I intermolecular interactions. The in-plane molecular rotation accompanied by a change in dipole moment resulted in dielectric phase transitions in polar dibromoiodomesitylene and dibromomesitylene crystals. No dielectric anomaly was observed for the in-plane molecular rotation of tribromomesitylene in the absence of this dipole moment change. Typical antiferroelectric−paraelectric phase transitions were observed in the dibromomesitylene crystal, whereas the dielectric anomaly of dibromoiodomesitylene crystals was associated with the collective in-plane molecular rotation of polar π-molecules in the π-stack. We found that the single-rope-like collective in-plane molecular rotator was dominated by intermolecular I···I interactions along the π-stacking column of polar dibromoiodomesitylene.

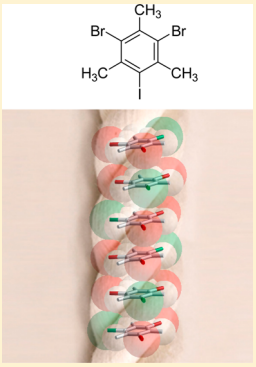

INTRODUCTION

Development of artificial molecular motors has been stimulated, in particular, by biological molecular motors such as ATPase and kinesin motors that can be used to conduct precise operations with high energy conversion efficiencies between chemical and kinetic energy.[1,2] Although the unidirectional motion of artificial molecular rotators such as triptycene-,[3] catenane-,[4] and rotaxane-based molecules[5] has been developed using intra- and intermolecular redox, acid−base, photothermal, and thermal reactions, the mechanical motion of these molecular systems is limited in the solution phase. Therefore, solid-state molecular rotators are key targets for realizing ideal molecular machines.[6,7]

Rotation of small structural units in a molecule, such as methyl groups in hexamethylbenzene crystals, can be thermally activated at room temperature as the long-range periodic molecular arrangement of the crystal has no effect on rotational motion.[8] In addition, large molecular rotations have been observed in plastic crystalline materials such as CCl_4, adamantane, and C_{60}, where the isotropic dynamic molecular rotations were observed in the absence of large steric hindrance.[9−11] The high-temperature dynamic rotator phase showed a phase transition to the low-temperature orientationally ordered static phase upon cooling, where the steric hindrance between the spherical molecules was small, even in the close-packing structures. However, the physical responses of plastic crystalline materials were largely unaffected by molecular rotations in symmetric apolar molecules. Therefore, targeted molecular design is important for developing functional molecular rotator systems.

Artificial solid-state molecular rotator−stator systems such as molecular gyroscopes,[12,13] metal−organic frameworks,[14] and supramolecular cationic systems[15] have been designed to achieve specific physical functions. Accurate molecular design for constructing rotator−stator systems is essential to achieve dynamic crystalline environments. For example, a two-dimensional rigid crystalline lattice using intermolecular I···I interactions has been utilized for constructing stator environments and fast rotator units with a rotary speed of 3 GHz at 300 K.[16] Another interesting chemical approach was reported in charge-transfer complexes based on disk-shaped aromatic hydrocarbons such as pyrene, perylene, and coronene, forming an in-plane molecular rotator along the direction normal to the π-plane.[17,18] The order−disorder-type antiferroelectric−paraelectric phase transition was observed in perylene tetrabromophthalic anhydride crystals, where the in-plane molecular rotation of the polar structure resulted in a phase transition to the low-temperature antiferroelectric state.[18]

We previously examined a two-fold flip-flop molecular rotator coupled with ferroelectric bulk physical properties in (*m*-FAni$^+$) (dibenzo[18]crown-6)[Ni(dmit)$_2$] crystal (dmit = 2-thioxo-1,3-dithiole-4,5-dithiolate).[19] The presence of the low-symmetry polar *m*-fluoroanilinium (*m*-FAni$^+$) cation resulted in different initial and rotated molecular structures with right and left dipole orientations, resulting in dipole inversion. The thermal activation of such dipole inversions above 346 K led to the ferroelectric−paraelectric phase transition, where the dipole

Received: August 17, 2015
Published: September 23, 2015

DOI: 10.1021/jacs.5b08215
J. Am. Chem. Soc. 2015, 137, 13155−13160

ordering ferroelectric state was achieved by the collective molecular rotation of *m*-FAni$^+$ cations arranging the crystal dipole moments. In contrast, the random molecular rotation of *m*-FAni$^+$ cations occurred in the high-temperature paraelectric phase.

Our next target is therefore achieving collective molecular rotation in molecular assemblies, which can be controlled by specific intermolecular interactions. Several types of intermolecular interactions are possible in simple disk-shaped π-molecules. We decided that the introduction of a dipole moment into the in-plane molecular rotation of such structures would enable us to clarify the relationship between dynamic molecular motions and dielectric responses in solid materials. We therefore report studies into halo (Br and/or I)-substituted mesitylene derivatives, namely, dibromoiodomesitylene (**1**), tribromomesitylene (**2**), dibromomesitylene (**3**), and diiodomesitylene (**4**) (Figure 1), whose phase transition behavior and

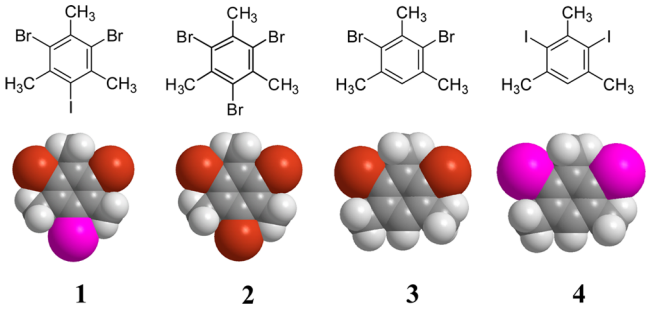

Figure 1. Molecular structures. Dibromoiodomesitylene (**1**), tribromomesitylene (**2**), dibromomesitylene (**3**), and diiodomesitylene (**4**). Bottom figures were drawn using the CPK model.

bulk physical properties are examined to investigate dynamic molecular behavior, intermolecular interactions, and dielectric responses coupled with in-plane molecular rotators. In addition, the intermolecular interactions between iodine atoms are investigated in terms of the collective molecular rotation in the dynamic rotator phase.

RESULTS AND DISCUSSION

The close-packing structures of **1**, **2**, **3**, and **4** were found to form van der Waals crystals, where $\pi-\pi$ and halogen−halogen interactions played an important role in constructing the crystal lattice and in the thermal stability of each crystal. The melting points of crystals **1**, **2**, **3**, and **4** were 475, 497, 337, and 355 K, respectively, while under ambient conditions, sublimation was observed before crystal melting (Figure S2). The initial differential scanning calorimetry (DSC) heating cycles for crystals **1** and **2** differed from the second thermal cycles, while no thermal changes were detected in the DSC cycle of crystal **3** (Figure 2). In the initial heating cycle, crystals **1** and **2** displayed irreversible endothermic peaks at approximately 380 and 360 K, with transition enthalpies (ΔH) of 2.68 and 2.62 kJ mol^{-1}, respectively. These transitions were assigned to the S1−M1 phase transition. Following the second thermal cycle, the reversible phase transitions of crystal **1** were observed at 358 K (heating) and 357 K (cooling), with a ΔH of ∼1.2 kJ mol^{-1} (Figure 2a). A trace of the endothermic peak was observed at ∼380 K even in the second heating cycle, which was dependent on the scan rate of the DSC measurements (Figure S3). The initial S1 phase of **1** was found to transform to the S2 phase following phase transition to the M1 phase. The first cooling

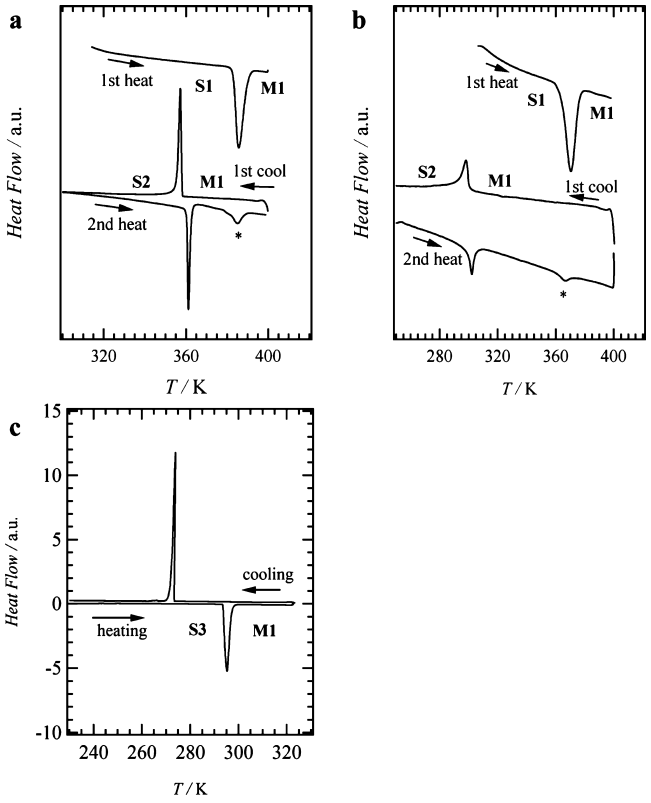

Figure 2. Phase transition behavior. DSC diagrams of crystals a) **1**, b) **2**, and c) **3**, with a scan rate of 5 K min^{-1}. Notation * signifies the phase transition of a trace amount of M1 phase in the second thermal cycle.

cycle from the M1 phase resulted in the formation of the crystalline S2 phase, which differed from the initial S1 phase. In the second heating cycle, the S2−M1 phase transition was reversible and was accompanied by a trace amount of S1−M1 phase transition at ∼380 K. Since the size of the small S1−M1 phase transition peak in the second heating cycle at a scan rate of 1 K min^{-1} was larger than that observed at 5 and 10 K min^{-1}, this suggested that the S1 phase was a thermodynamically stable crystal phase. The phase transition behaviors of all crystals were reproducible following the second thermal cycle in DSC and dielectric measurements.

Similar phase transition behavior was observed for crystal **2**, with the reversible S2−M1 transition being observed at 298 K (heating) and 288 K (cooling), respectively, with a ΔH of ∼0.7 kJ mol^{-1} (Figure 2b). The S1 phase was also detected in the second DSC cycle as a small endothermic peak. The S2−M1 transition temperature and ΔH magnitude of **2** were, respectively, ∼60 K and 0.5 kJ mol^{-1} lower than those of **1**, suggesting intermolecular interactions in crystal **1** that are weaker than that in crystal **2**.

In crystal **3**, the reversible S3−M1 phase transition upon heating and cooling was observed at 294 K (ΔH = 7.74 kJ mol^{-1}) and 273 K (ΔH = 8.05 kJ mol^{-1}), respectively, accompanying a relatively large thermal hysteresis (>20 K in Figure 2c). This thermal hysteresis in the heating and cooling processes was not observed in the S2−M1 phase transitions of **1** or **2**, and it was assumed that **3** showed first-order transition behavior from ordered solid (S3) to plastic crystalline phase (M1).

DOI: 10.1021/jacs.5b08215
J. Am. Chem. Soc. 2015, 137, 13155−13160

In contrast, crystal **4** did not exhibit any phase transition from the solid to the mesophase, displaying only a direct transformation to the isotropic liquid state. The replacement of two bromine atoms in **3** with iodine atoms (**4**), therefore, resulted in the disappearance of the S3−M1 phase transition and an increase in the melting point by ∼20 K. This suggested that the intermolecular interactions between I atoms in the crystals were stronger than those between Br atoms. Other effective intermolecular C−H···I (Br) interactions also played an important role to generate the attractive force in solids.[16b]

Figure 3 shows the polarized optical microscopic (POM) images of crystals **1** and **2** with a cross-Nichol optical

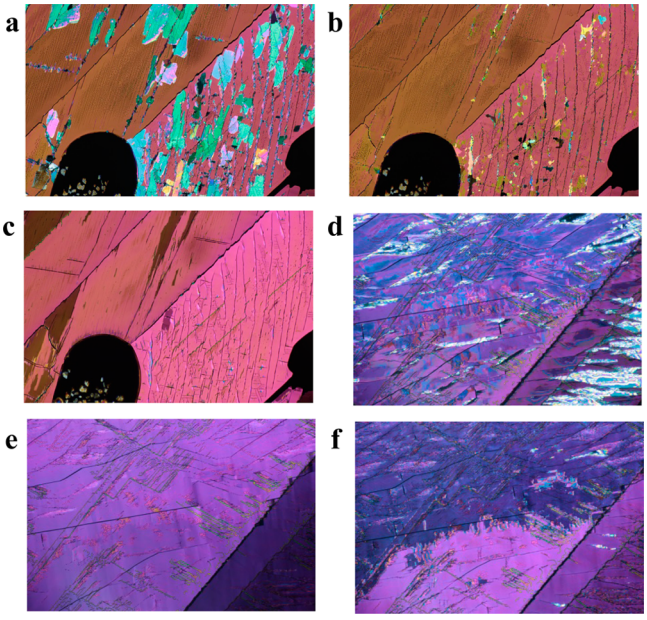

Figure 3. Polarized optical microscopic images of crystals **1** and **2**. Phase transition behavior of crystal **1** between (a) S1 (T = 370 K), (b) M1 (T = 400 K), and (c) S2 (T = 300 K) phases. Phase transition behavior of crystal **2** between (d) S1 (T = 300 K), (e) M1 (T = 380 K), and (f) S2 (T = 300 K) phases.

arrangement. The green/blue mosaic domains of **1** in the S1 phase (T = 370 K) were not present in the M1 phase (400 K), while a uniform pink domain was observed in the S2 phase when the temperature was decreased to 300 K (Figure 3a−c). Similar phase transition behavior was also observed in the POM images of **2**. The blue/violet mosaic domains in the S1 phase (T = 300 K) changed to uniform violet domains in the M1 phase (T = 380 K) and uniform pink/violet domains in the S2 phase (T = 300 K), as shown in Figure 3d−f. The POM images of **3** also displayed changes in the domain shape and color around the S3−M1 phase transition (Figure S4).

Structural analysis by single-crystal X-ray diffraction of the S1 phase of crystal **1** was only successful upon cooling of the crystals (Figure 4a−d), and the thermal cycle of **1** through the M1 phase was particularly damaging to the crystalline S2 phase. The crystallographically independent $C_9H_9Br_2I$ unit was found to have the $P\bar{1}$ centric space group in the S1 phase of crystal **1**. The previously reported crystal structure of **2** at 173 K[20] was found to be isostructural to that of **1** at 100 K. The orientational disorder for two Br and one I atom was observed as an average molecular structure (Figure 4a,b). The typical C−Br and C−I bond lengths in the aromatic compounds have previously been reported as 1.85 and 2.05 Å, respectively.[21] In

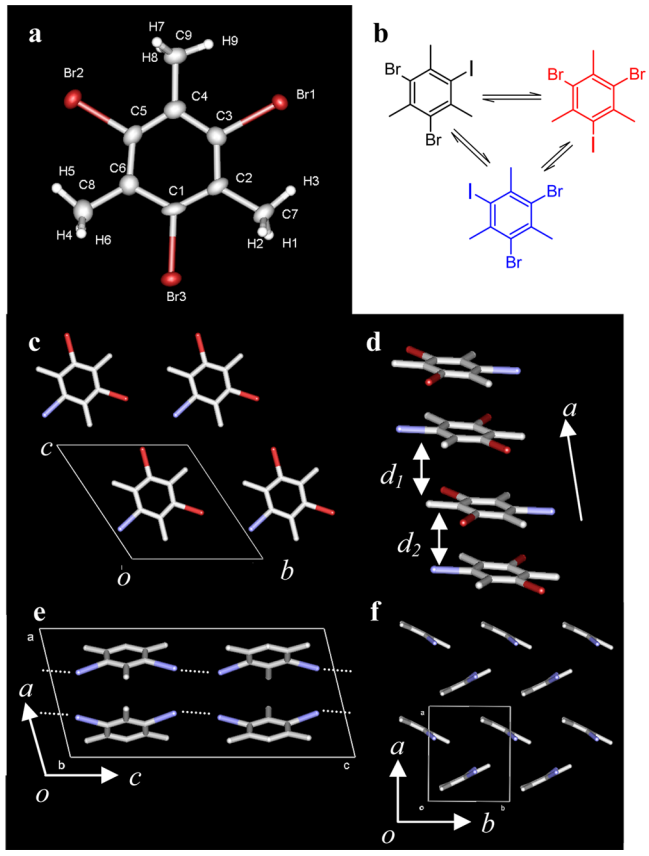

Figure 4. Crystal structures of the S1 phase of **1** and **4** (T = 100 K). (a) Average molecular structure for orientationally disordered Br and I atoms. (b) Three possible molecular orientations were possible with every 120° rotation of the benzene ring along the direction normal to the π-plane. (c) Unit cell of crystal **1** viewed along the a axis. The I atom was ideally assigned at the position of Br3 atom. (d) π-Stacking structure of molecule **1** along the a axis. Two types of interplanar interactions were observed. (e) Unit cell of **4** viewed along the b axis. The I···I interaction (represented by dashed lines) was elongated along the c axis. (f) Herringbone arrangement of **4** within the ab plane, where molecule **4** was oriented in the ferroelectric arrangement. Hydrogen atoms are omitted for clarity.

addition, the bond lengths of Br1−C3, Br2−C5, and Br3−C1 in **1** were found to be 1.980(6), 1.988 (9), and 2.017(7) Å, respectively (Figure 4a), which are consistent with the average bond lengths of two C−Br and one C−I bond. Although all molecular motions should be frozen at 100 K, the dynamic disordered state for the orientation of Br and I atoms was expected in the high-temperature M1 phase. The temperature-dependent powder X-ray diffraction (PXRD), DSC, and dielectric measurements of **1** strongly supported the dynamic orientational disorder of Br and I atoms in the M1 phase.

Figure 4c shows the unit cell of crystal **1** viewed along the a axis, where iodine was ideally assigned at the position of the Br3 atom to clarify the molecular orientation. The length of the b axis (9.2673(3) Å) was 0.02 Å shorter than that of the c axis (9.2879(3) Å), suggesting broken symmetry and anisotropic molecular orientation at 100 K. Nonuniform π-stacking structure was observed along the a axis of **1** (Figure 4d), where the two types of interplanar distances, d_1 = 3.64 and d_2 = 3.66 Å, were defined by the mean interplanar distances between the two benzene planes. The nonuniform π-stacking structure of **1** was associated with a significant H···H interaction between

DOI: 10.1021/jacs.5b08215
J. Am. Chem. Soc. 2015, 137, 13155−13160

$-CH_3$ groups, which affected the dynamic behavior of individual molecules and the magnitude of rotational barriers as the repulsive interaction.[16b] Since the X-ray diffuse scattering of **1** from the superstructure of the heavy iodine arrangement was not observed in the S1 phase, the disordered iodine atoms were distributed three positions in the lattice.

The isostructural crystal structure of **2** at 173 K showed a ~5% contraction of the unit cell volume compared to that of **1** due to the replacement of an I atom with a smaller Br atom. Orientational disorder of Br atoms was not observed in crystal **2**. It was difficult to obtain high-quality diffraction data in the single-crystal X-ray analysis of **3** due to a phase transition at room temperature. However, the PXRD patterns of **3** at 263 K were consistent with that of the S3 phase of **4** (Figures S7 and S8), indicating a similar herringbone packing structure. In addition, the S3−M1 phase transition of **3** at 294 K upon heating was suppressed in **4**. The PXRD pattern of the S2 phase in crystal **1** was dependent on the annealing procedures due to the coexistence of the S1 phase. Since similar intermolecular interactions and packing structures were expected in these two crystals, we then chose to examine the crystal structure of **4**. Figure 4e,f shows the unit cell of crystal **4** viewed along the *b* and *c* axes, respectively. A single $C_9H_{10}I_2$ molecule was the crystallographically independent structural unit, where two C−I bonds of 2.116(6) and 2.109(7) Å were observed in the orientationally ordered state at 100 K. The herringbone packing structure in **4** was observed in the *ab* plane, as opposed to the π-stacking structure of **1** and **2**. The ferroelectric molecular orientation of **4** in the *ab* plane was alternately arranged along the *c* axis to cancel the total dipole moment with the antiferroelectric arrangement (Figure S6). In addition, the effective I···I interaction (3.945(2) Å) was uniformly elongated along the *c* axis, which enhanced the intermolecular interactions and thermal stability of **4**, thus resulting in the absence of the S3−M1 phase transition. Since the magnitude of the Br···Br interaction was lower than that of I···I,[22] the in-plane molecular rotation of **3** could be thermally activated at relatively low temperatures (~280 K). Furthermore, the motional freedom of **3** differed from those in π-stacking molecules **1** and **2**, which was consistent with the difference in the phase transition behavior observed in the DSC traces.

Based on density functional theory (DFT) calculations, the in-plane dipole moments of **1**, **2**, **3**, and **4** were found to be 0.13, 0, 1.28, and 1.44 D, respectively. The dielectric constant of $\varepsilon = \varepsilon_1 + i\varepsilon_2$ was sensitive to the dipole change in solids, where the ε_1 and ε_2 corresponded to the real and imaginary parts. The former ε_1 drastically changed at dielectric phase transitions such as ferroelectric and/or antiferroelectric−paraelectric ones. The motional freedom of apolar molecule **2** could not be detected in the dielectric spectra as no change in dipole moment took place (Figure S8). Figure 5a,b shows the temperature- and frequency-dependent real part dielectric constant (ε_1) of single-crystal **1** and the compressed pellet **3**. The π-stacking direction of crystal **1** along the *a* axis was silent for the dielectric measurement, whereas the ε_1 response along the *bc* plane normal to the π-stacking axis showed a clear ε_1 response. This is consistent with the in-plane molecular rotation of polar molecule **1** within the π-stacking column. The S1−M1 phase transition of **1** appeared as a sharp drop in the ε_1 measurement at 380 K along the *bc* plane upon heating, whereas the dielectric ε_1 jump was observed at 360 K in the cooling cycle at the M1−S2 phase transition. It should be noted

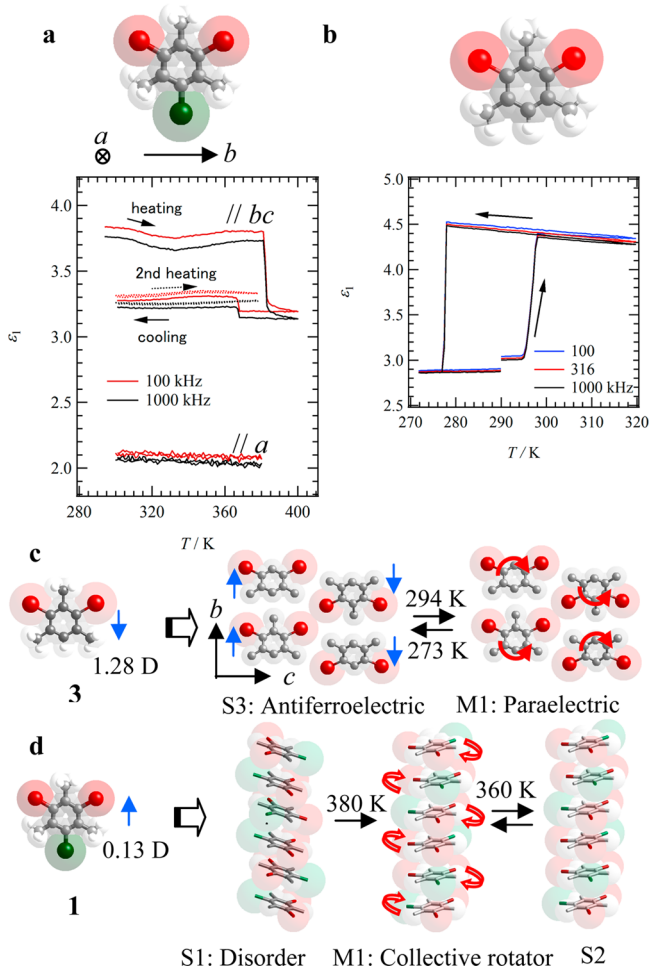

Figure 5. Temperature- and frequency-dependent real part dielectric constants (ε_1) and phase transition mechanism. (a) Two types of measurement axes along the *a* axis and the *bc* plane corresponded to the parallel and normal π-stacking axis of single-crystal **1**, respectively. The second thermal cycles were plotted as dashed lines in the absence of ε_1 anomaly and thermal hysterics. (b) Phase transition of compressed pellet **3** from the low-temperature antiferroelectric phase to the high-temperature paraelectric phase. (c) Phase transition from the antiferroelectric static ordered S3 phase to the paraelectric dynamic disordered M1 phase, accompanied by thermal hysteresis. (d) Static disordered π-stacking columnar structure of polar molecule **1**, where the orientation of iodine atoms was disordered, generating the macro dipole moment and dipole fluctuation. Phase transition from the static disordered S1 phase to the dynamic collective rotator phase M1 occurred at 380 K, and the static ordered S2 phase was formed from the M1 phase upon cooling.

that the ε_1 anomaly was not observed in the second thermal cycle (300−380 K), although the reversible S2−M1 phase transition was clearly observed at 360 K by DSC measurements. The in-plane molecular rotation of **1** in the π-stacking column exhibited a change in dipole moment at the S1−M1 phase transition but not at the S2−M1 transition.

The temperature- and frequency-dependent ε_1 of **3** was found to be in accordance with the DSC measurements. A rapid ε_1 jump from 3.0 to 4.3 occurred at 295 K upon heating, while a sudden drop was observed at 278 K upon cooling. In addition, the frequency-independent reversible dielectric phase transition corresponded to dielectric ordering at the S3−M1 phase transition temperature, where the low-temperature antiferroelectric phase transformed to the high-temperature

DOI: 10.1021/jacs.5b08215
J. Am. Chem. Soc. 2015, 137, 13155−13160

paraelectric one. Furthermore, the thermally activated in-plane molecular rotation of **3** in the M1 phase resulted in the high-temperature dynamic disordered paraelectric phase being observed in the herringbone packing structure. The in-plane molecular rotation was found to be suppressed by Br···Br interactions in the S3 phase, forming an antiparallel molecular arrangement to cancel the net dipole moment in the crystal. It was therefore clear that the dielectric responses of **1** and **3** were not comparable.

The dielectric phase transition mechanism of **1** and **3** was discussed in terms of the rotational freedom and packing structures. The phase transition of **3** showed a typical temperature-dependent dielectric response from the antiferroelectric to paraelectric phases (Figure 5c). The larger dipole moment of **3** compared to that of **1** effectively stabilized the antiparallel molecular arrangement and canceled the net dipole moment of the crystal. The ferroelectric dipole arrangement of polar **3** was observed in the *ab* plane, which interacted with the antiparallel dipole arrangement along the interlayer *c* axis. An increase in temperature up to 294 K generated the in-plane molecular rotation and formed the paraelectric phase. The independent in-plane molecular rotations of **3** contributed to the dielectric phase transition in the absence of π-stacking interactions, with Br···Br interactions playing an important role in revealing the antiferroelectric−paraelectric phase transition.

The temperature-dependent dielectric response of **1** exhibited rather complex behavior. An increase in temperature from the S1 phase resulted in a sudden drop in ε_1 at the S1−M1 phase transition temperature, which was not consistent with typical antiferroelectric−paraelectric phase transition behavior. Furthermore, no ε_1 responses were observed following the second thermal cycles despite **1** exhibiting a permanent dipole moment. Since the dipole−dipole interaction between the molecules of **1** was smaller than that of molecule **3**, both the π-stacking interactions and steric hindrance within the π-stack played an important role in determining the dielectric phase transition behavior. The sudden drop in ε_1 at the S1−M1 phase transition was associated with the existence of intrinsic static disorder of I atoms in the S1 π-stack, where the orientationally disordered I atom enhanced the polarization magnitude and ε_1 values (Figure 5d). The in-plane molecular rotation of **1** in the M1 phase relaxed the intrinsic orientational disorder of I atoms and resulted in a sudden drop in ε_1 at 380 K. Cooling from the M1 to the S2 phase fixed the orientation of the I atoms of **1** in the π-stack, resulting in the disappearance of the net dipole moment of one π-stacking column. The dielectric anomaly at the S2−M1 phase transition was found to disappear in the absence of the dipole moment change, due to the collective in-plane rotation of **1** in the π-stack, resulting in constant ε_1 values at this phase transition. A helical arrangement of **1** was possible, with 3_1 symmetry along the π-stack, where I···I interactions maintained each molecular orientation. The I···I distance of ∼4.2 Å for the 3_1-helix arrangement of **1** in the π-stack resulted in a collective in-plane molecular rotation in the π-stacking column. The weaker Br···Br interaction is not sufficient to achieve a collective in-plane molecular rotation of **2** in the π-stacking column. Therefore, the dynamic M1 phase of **1** was considered to be the collective ordered π-stacking rotator phase, where the molecular orientation was collectively activated in a single-rope-like long-range assembly.

CONCLUSIONS

The phase transition from the static solid phase to the thermally activated dynamic in-plane rotator phase was activated by molecular rotation along the direction normal to the crystal π-plane. The isostructural crystal structures of **1** and **2** indicated the formation of a π-stacking columnar structure, whereas a herringbone molecular arrangement was observed for crystal **4**. Effective I···I interactions in **4** suppressed the phase transition to the in-plane rotator phase, whereas the weak Br···Br interactions in **3** resulted in the formation of the rotator phase before crystal melting occurred. No dielectric response was observed in apolar molecule **2** due to in-plane rotations, whereas those of asymmetric polar molecules **1** and **3** were responsible for their temperature- and frequency-dependent dielectric spectra. Typical antiferroelectric−paraelectric phase transition behavior was observed in the temperature-dependent ε_1 of **3**, whereas the temperature-dependent ε_1 of **1** could be accounted for by phase transition from the static disordered phase to the dynamic ordered collective rotator phase. In this case, the in-plane molecular rotation was collectively activated in the π-stacking columnar structure, and macro dipole moments were canceled out. Dipole relaxation from the static disordered low-temperature phase to the dynamic ordered collective in-plane rotator phase resulted in a dielectric anomaly in **1** during the first heating cycle, with the collective in-plane molecular rotation of **1** occurring in a single-rope-like π-stacking columnar assembly. No correlation was observed between the molecular rotator columns, and the realization of collective in-plane rotation for all columns in the bulk has the potential to achieve unidirectional molecular motion for constructing molecular motors in the future.

METHODS

Preparation and Physical Measurements. Compounds **1**, **2**, **3**, and **4** were prepared according to literature methods.[20,23] Single crystals for X-ray structural analysis were grown by vacuum sublimation at 130 °C under 5−10 Pa. Differential scanning calorimetry was carried out using a Rigaku Thermo Plus TG8120 thermal analysis station with Al_2O_3 reference under N_2. Temperature-dependent dielectric constants were measured using the two-probe AC impedance method between 100 and 1000 × 10^3 Hz (HP 4194A impedance/gain-phase analyzer, Hewlett-Packard). Electrical contacts were prepared using gold paste (Tokuriki 8560) to attach the 10 μm ϕ gold wires to the single crystal and the 25 μm ϕ gold wires to the 3 mm ϕ compressed pellet. Temperature control between 300 and 400 K was carried out using a Linkam LTS350 hot stage.

Crystal Structure Determination. Temperature-dependent crystallographic data for crystals **1** and **4** (Table S1) were collected using a Rigaku RAPID-II diffractometer equipped with a rotating anode and fitted with a multilayer confocal optic using Cu Kα (λ = 1.54187 Å) radiation from a graphite monochromator. Structural refinements were carried out using the full-matrix least-squares method on F^2. The crystal structure data for **1** and **4** can be accessed from the Cambridge Crystallographic Data Centre (CCDC, www.ccdc.cam.ac.uk) and have been allocated accession numbers CCDC 1406424 and 1406425.

Calculations. The dipole moments of molecules **1**, **2**, **3**, and **4** were obtained by DFT calculations using the B3LYP 6-31G(d,p) basis set in Gaussian 09W.[24] The potential energy curves for the in-plane rotations of molecules **1**, **2**, and **4** were obtained in the atomic coordinates based on the single-crystal X-ray structural analyses. The calculations were performed for the π-trimer units of $(\mathbf{1})_3$ and $(\mathbf{2})_3$, whereas the rotation of **4** was examined on the partial herringbone arrangement structure of the $(\mathbf{4})_3$ unit. The single-point energy was obtained at 30° rotation intervals from the central molecules based on an RHF/6-31(d,p) basis set.

DOI: 10.1021/jacs.5b08215
J. Am. Chem. Soc. 2015, 137, 13155−13160

■ ASSOCIATED CONTENT

Supporting Information

The Supporting Information is available free of charge on the ACS Publications website at DOI: 10.1021/jacs.5b08215.

IR spectra on KBr pellet, TG charts, POM images of **3** and **4**, DSC charts of **1** at different scan rates, crystal structure of **4**, dielectric properties of **1**, **2**, and **4** on a compressed pellet, PXRD pattern of **4**, potential energy calculation for **1** with different orientations (PDF)

X-ray data (CIF)

■ AUTHOR INFORMATION

Corresponding Author

*akuta@tagen.tohoku.ac.jp

Notes

The authors declare no competing financial interest.

■ ACKNOWLEDGMENTS

This work was supported by a Grant-in-Aid for Science Research from the Ministry of Education, Culture, Sports, Science, and Technology of Japan, and by a grant from the Management Expenses Grants for National Universities of Japan.

■ REFERENCES

(1) Yasuda, R.; Noji, H.; Kinosita, K., Jr; Yoshida, M. *Cell* **1998**, *93*, 1117−1124.

(2) Astumian, R. D. *Science* **1997**, *276*, 917−922.

(3) Koumura, N.; Zijlstra, R. W. J.; van Delden, R. A.; Harada, M.; Feringa, B. L. *Nature* **1999**, *401*, 152−155.

(4) Leigh, D. A.; Wong, J. K. Y.; Dehez, F.; Zerbetto, F. *Nature* **2003**, *424*, 174−179.

(5) Schalley, C. A.; Beizai, K.; Vögtle, F. *Acc. Chem. Res.* **2001**, *34*, 465−476.

(6) Khuong, T.-A. V.; Nuñez, J. E.; Godinez, C. E.; Garcia-Garibay, M. A. *Acc. Chem. Res.* **2006**, *39*, 413−422.

(7) Akutagawa, T.; Nakamura, T. *Dalton Trans.* **2008**, 6335−6345.

(8) Atake, T.; Gyoten, H.; Chihara, H. *J. Chem. Phys.* **1982**, *76*, 5535−5540.

(9) Sherwood, J. N. *The Plastically Crystalline State*; John Wiley & Sons: Chichester, U.K., 1979.

(10) Chang, S.-S.; Westrum, E. F., Jr. *J. Phys. Chem.* **1960**, *64*, 1547−1551.

(11) Johnson, R. D.; Yannoni, C. S.; Dorn, H. C.; Salem, J. R.; Bethune, D. S. *Science* **1992**, *255*, 1235−1238.

(12) Garcia-Garibay, M. A. *Proc. Natl. Acad. Sci. U. S. A.* **2005**, *102*, 10771−10776.

(13) Shima, T.; Hampel, F.; Gladysz, J. A. *Angew. Chem., Int. Ed.* **2004**, *43*, 5537−5540.

(14) Gould, S. L.; Tranchemontagne, D.; Yaghi, O. M.; Garcia-Garibay, M. A. *J. Am. Chem. Soc.* **2008**, *130*, 3246−3247.

(15) (a) Nishihara, S.; Akutagawa, T.; Sato, D.; Takeda, S.; Noro, S.; Nakamura, T. *Chem. - Asian J.* **2007**, *2*, 1083−1090. (b) Fu, D.-W.; Zhang, W.; Cai, H.-L.; Zhang, Y.; Ge, J.-Z.; Xiong, R.-G.; Huang, S. D. *J. Am. Chem. Soc.* **2011**, *133*, 12780−12786. (c) Fu, D.-E.; Cai, H.-L.; Li, S.-H.; Ye, Q.; Zhou, L.; Zhang, W.; Zhang, Y.; Deng, F.; Xiong, R.-G. *Phys. Rev. Lett.* **2013**, *110*, 257601.

(16) (a) Lemouchi, C.; Vogelsberg, C. S.; Zorina, L.; Simonov, S.; Batail, P.; Brown, S.; Garcia-Garibay, M. A. *J. Am. Chem. Soc.* **2011**, *133*, 6371−6379. (b) Lemouchi, C.; Yamamoto, H. M.; Kato, R.; Simonov, S.; Zorina, L.; Rodríguez-Fortea, A.; Canadell, E.; Wzietek, P.; Iliopoulos, K.; Gindre, D.; Chrysos, M.; Batail, P. *Cryst. Growth Des.* **2014**, *14*, 3375−3383.

(17) Yoshida, Y.; Kumagai, Y.; Mizuno, M.; Saito, G. *Cryst. Growth Des.* **2015**, *15*, 1389−1394.

(18) Harada, J.; Ohtani, M.; Takahashi, Y.; Inabe, T. *J. Am. Chem. Soc.* **2015**, *137*, 4477−4486.

(19) Akutagawa, T.; Koshinaka, H.; Sato; Takeda, S.; Noro, S.; Takahashi, H.; Kumai, R.; Tokura, Y.; Nakamura, T. *Nat. Mater.* **2009**, *8*, 342−347.

(20) Ghanemi, S.; Hernandez, O.; Boudjada, A.; Meinnel, J. *Acta Crystallogr., Sect. C: Cryst. Struct. Commun.* **2009**, *C65*, o498−o501.

(21) Allen, F. H.; Kennard, O.; Watson, D. G.; Brammer, L.; Orpen, A. J. *J. Chem. Soc., Perkin Trans. 2* **1987**, S1−S19.

(22) Pedireddi, V. R.; Reddy, D. S.; Goud, B. S.; Craig, D. C.; Rae, A. D.; Desiraju, G. R. *J. Chem. Soc., Perkin Trans. 2* **1994**, 2353−2360.

(23) Kajigaeshi, S.; Kakinami, T.; Moriwaki, M.; Tanaka, T.; Fujisaki, S.; Okamoto, T. *Bull. Chem. Soc. Jpn.* **1989**, *62*, 439−443.

(24) Frisch, M. J.; et al. *Gaussian 09*, revision C 01; Gaussian, Inc.: Wallingford, CT, 2009.

DOI: 10.1021/jacs.5b08215
J. Am. Chem. Soc. 2015, 137, 13155−13160